

Article

Quantitative Characterization and Controlling Factors of Shallow Shale Reservoir in Taiyang Anticline, Zhaotong Area, China

Kai Ma ^{1,2}, Bing Zhang ^{1,2,3,*}, Siyu Wen ^{1,2}, Xiaoyang Lin ³, Yan Wang ³ and Kai Yang ³¹ Institute of Sedimentary Geology, Chengdu University of Technology, Chengdu 610000, China² State Key Laboratory of Oil and Gas Reservoir Geology and Exploitation, Chengdu 610000, China³ School of Geophysics, Chengdu University of Technology, Chengdu 610000, China

* Correspondence: zhangb@cdut.edu.cn

Abstract: Pore and its structural characteristics are key parameters affecting shale gas reservoir development. Accurate quantitative characterization of shale pore and its structural characteristics is of great significance for evaluating shale reservoir state. In this study, 15 shallow marine shale samples were collected in Well Y108. X-ray diffraction results indicate that brittle minerals are the most common components in shale. In this paper, various pore types are classified and characterized by scanning electron microscope images. The total porosity of shale measured by the mercury intrusion method is between 3.2% and 6.5%. In addition, a petrophysical model is established to calculate matrix porosity and fracture. The results of this model are consistent with the measured porosity. Three key parameters ($V_{TOC} > V_{Bri} > V_{Clay}$) were obtained. The low-pressure N_2/CO_2 adsorption experiment allows for the analysis of pore volume, specific surface area, and pore size. Finally, it was determined that the primary pore types and primary shale gas reservoir space in shallow marine shale are mesopores and micropores. The impact of shale constituents on pores and their structural properties is also covered in this work. The results indicate that the enrichment of total organic carbon and brittle minerals is conducive to the development of shallow marine shale pore-fracture system. Additionally, there is a positive linear relationship between matrix porosity, pore volume, specific surface area, average pore diameter, and surface porosity.

Keywords: shallow shale; Wufeng–Longmaxi formation; pore-fracture system; quantitative characterization; controlling factors



Citation: Ma, K.; Zhang, B.; Wen, S.; Lin, X.; Wang, Y.; Yang, K.

Quantitative Characterization and Controlling Factors of Shallow Shale Reservoir in Taiyang Anticline, Zhaotong Area, China. *Minerals* **2022**, *12*, 998. <https://doi.org/10.3390/min12080998>

Academic Editor: Samintha Perera

Received: 17 June 2022

Accepted: 2 August 2022

Published: 8 August 2022

Publisher's Note: MDPI stays neutral with regard to jurisdictional claims in published maps and institutional affiliations.



Copyright: © 2022 by the authors. Licensee MDPI, Basel, Switzerland. This article is an open access article distributed under the terms and conditions of the Creative Commons Attribution (CC BY) license (<https://creativecommons.org/licenses/by/4.0/>).

1. Introduction

Natural gas has increasingly become the primary energy consumption in China, thanks to the rapid increase in the country's energy demand, and shale gas, one of the natural gas sources, being plentiful [1]. Scholars have discovered that shale varies from traditional carbonate and sandstone reservoirs with micron-sized pores as the investigation and development of shale reservoirs proceeds [2]. The pore system of shale is more complex and diverse. Pore type, shape, and distribution directly affect the quality and migration of shale gas reservoirs [3]. Therefore, the quantitative characterization of shale pore fracture system plays an important role in explaining shale gas occurrence and flow mechanism, estimating shale gas reservoir capacity, and studying migration kinetics.

Scholars have proposed a variety of research approaches in recent years to analyze the complex and diversified pore-fracture system (PFS) of shale reservoirs [4,5]. Researchers employed the fluid adsorption approach to determine the pore-fracture system parameters of porosity, permeability, pore-volume (PV), specific surface area (SSA), and pore size (PSD) [6–9]. Computer tomography (CT), field emission/scanning electron microscopy (FE-SEM/SEM), transmission electron microscopy (TEM), and focused ion beam scanning electron microscopy (FIB-SEM) were utilized to examine the pore-fracture type, shape, size, and distribution. Furthermore, shale pore properties have been studied using nuclear magnetic resonance (NMR) and ultra-small angle neutron scattering (USANS/SANS) [10].

In recent years, studies have found that Zhaotong National Demonstration Zone is primarily located in the residual depression area of complex structures outside Sichuan Basin, and shallow shale gas exploration evaluation is performed in the Taiyang anticline structural trap area [11,12]. After that, many scholars performed preliminary analysis and research on the formation conditions and sweet spot control factors of shallow shale gas in the Zhaotong Taiyang anticline, which promotes the exploration and development of shallow marine shale gas in southern China [13]. Moreover, in the study of pore structure of shale reservoirs with different burial depths, it is discovered that there are obvious differences in pores between deep and shallow shale reservoirs [14]. The Zhaotong National Demonstration Area is the key area of shale gas exploration and development in the Sichuan Basin. Predecessors have performed much research on the accumulation mode, preservation conditions, and development methods of shallow marine shale in this area [15–19]. However, the Zhaotong area is located in the complex marine structure area in southern China. The shale deformation and transformation are strong, and the influence on shale pores is obvious [20]. Additionally, in the Taiyang anticline in the Zhaotong area, the quantitative characterization of pore fractures and the primary regulatory variables of pore production are rather weak. Therefore, the study of pores in Zhaotong area performs a very important role. The organic matter content and mineralogical features of the Shallow marine shale in the Zhaotong area were investigated in this study. The shale pore fracture system was interpreted using FE-SEM images, N₂ gas adsorption, CO₂ gas adsorption, high-pressure mercury intrusion porosimetry (HMIP), and shale pore-fracture petrophysical models. The goal of this research is to describe the pore-fracture system (PFS) of the Zhaotong area Taiyang anticline in both qualitative and quantitative terms. We also aim to use the relationship between total organic carbon (TOC) content, mineral fraction, pore-volume, specific surface area, matrix porosity, and other parameters to comprehensively explore the primary governing factors of the pore-fracture system. This study is of great significance to the exploration of shallow shale gas development in the Taiyang anticline in the Zhaotong area.

2. Materials and Methods

2.1. Materials

The Zhaotong shale gas development demonstration area is situated in the transition zone between the southern Sichuan basin's low-steep folded belt and the northern Yunnan–Guizhou depression [21]. The marine shales of the Longmaxi Formation in this location are part of the same deep-water shelf-phase depositional environment as the adjacent Changning, Weiyuan, and Jiao Shiba shales in the southern Sichuan–Chongqing region [22]. The sample collection area is primarily located in Zhaotong–Gulin syncline in Zhaotong shale gas development demonstration area, which is the first structural unit to obtain exploration breakthroughs in shallow shale gas [23].

The experimental samples were obtained from appraisal well Y108 in the Zhaotong National Shale Gas Demonstration Area's Taiyang anticline, with the sampling point illustrated in Figure 1. Shale samples were obtained from the Wufeng–Longmaxi Formation's organic-rich shale layer, totaling 15 samples at a depth of 2382.4–32512.15 m. The following three principles are followed in the sampling process to ensure the validity of the test results:

- (1) Avoiding the fracture development site;
- (2) To avoid severely weathered surfaces, we selected fresh shale samples;
- (3) Shale hand specimens with high organic matter content were selected.

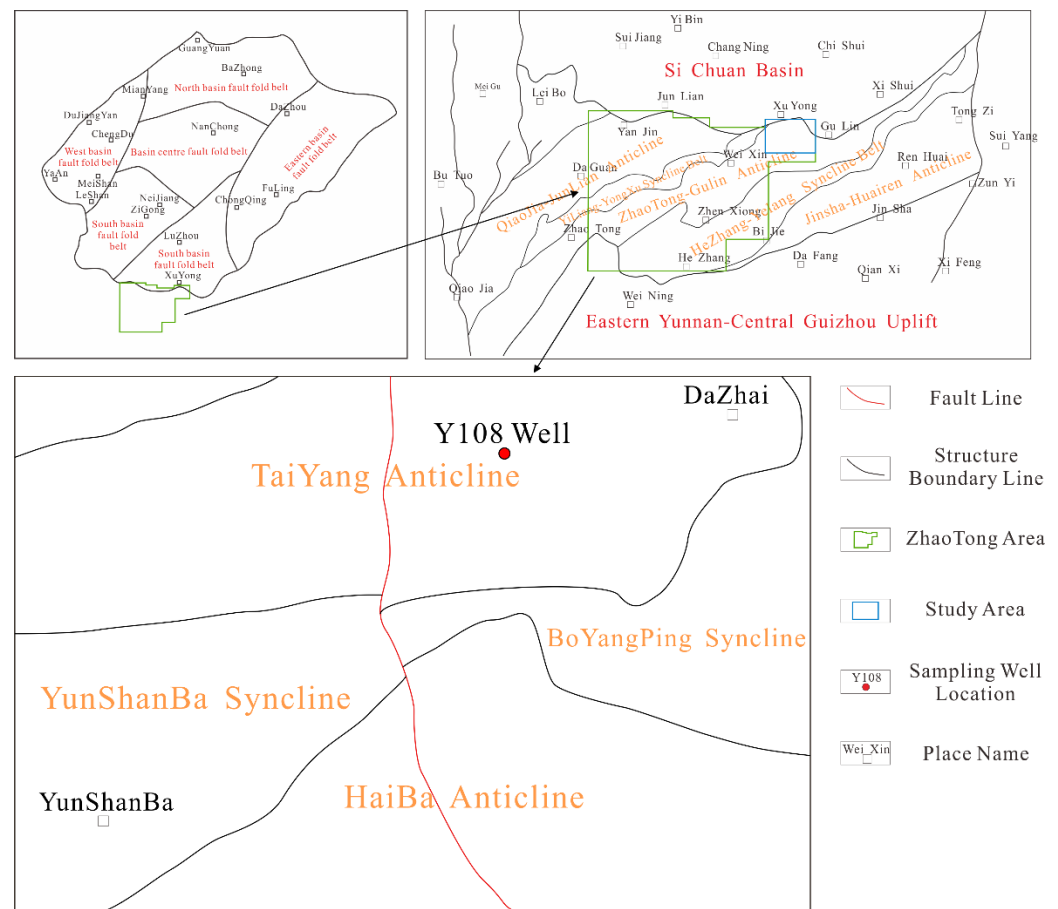


Figure 1. Structural map and sampling well location of Wufeng–Longmaxi Fm in Zhaotong area.

2.2. Methods

2.2.1. FE-SEM Characterization

Using ultra-high image resolution, FE-SEM can efficiently determine shale pore types and shapes. Before scanning, shale samples were first treated to 1 cm² scanning electron microscope slices. Secondly, the Sputter Coaster (Emitech K550X, Montigny-le-Bretonne, France) argon ion grinding instrument was used to uniformly plate gold on the surface of the sample to enhance its surface conductivity and obtain higher-quality images. Finally, Quanta250FEG (FEI, Hillsboro, OR, USA) (working conditions: accelerating voltage: 20 kV, enabling: 50 to 300,000 times) was used to scan the samples at 24 °C and 35% humidity. An energy spectrometer (INCAx-max20, Oxford, Oxford, UK) was utilized for elemental analysis during the experiment to confirm the accuracy of mineral identification. The experiment was completed in the State Key Laboratory of Oil and Gas Reservoir Geology and Exploitation, Chengdu University of Technology.

2.2.2. Pore Characteristics Determination

Low-Pressure Gas Adsorption

The adsorption/desorption experiments of low-pressure N₂/CO₂ gas were performed at the Beijing Center for Physical and Chemical Analysis (BCPCA) using an ASAP 2460 four-station automatic rapid specific surface area and pore analyzer (Micromeritics, Norcross, GA, USA).

Before analysis, shale samples were sieved to obtain grain sizes of 40–60. Then the samples were vacuum degassed at 150 °C to remove moisture and other pollutants. Gas adsorption-desorption isotherms were obtained for all samples under relative pressures (P/P₀) ranging from 0.01 to 0.993 at 77 K.

Mercury Intrusion Porosimetry

According to the national standard GB/T21650.2-2008 [24], Pore MasterGT60 mercury injection equipment (Quantachrome Instruments, Boynton Beach, FL, USA) was used to measure mercury intrusion in samples at Beijing Physical and Chemical Analysis Center (BCPCA). The measured pressure range is 0 to 60,000 psi. PSD is calculated by the Washburn equation [25].

Mercury Intrusion Porosimetry

Scholars have presented a significant variety of petrophysical models to explore pore cracks in layered shale reservoirs. A rock skeleton layer, clay mineral layer, organic matter layer, and pore layer were postulated by LeCompte [26] as part of a four-layer petrophysical model. Wang et al. [27] created a three-layer petrophysical model with a brittle mineral layer, clay mineral layer, and organic matter layer, but the cracks in the rocks were overlooked in the model. Zhang et al. [28] created a four-layer petrophysical model that included brittle minerals, clay minerals, organic matter, and fracture layers (Figure 2).

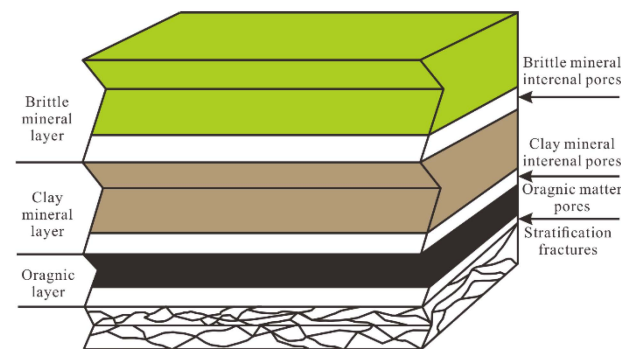


Figure 2. Physical layered model of the shale rock structure.

The pores in shale are primarily divided into matrix pores and fractures, and matrix pores include brittle mineral pores, organic pores, and clay mineral pores. The matrix pores are the primary reservoir space of shale reservoirs [29]. Its quantitative characterization must reflect the contribution of brittle minerals (quartz, attempt, and carbonate minerals), organic matter, and clay minerals to reservoir space.

$$\varphi_{Total} = \varphi_{Matrix} + \varphi_{Frac} \quad (1)$$

$$\varphi_{Matrix} = \rho \times A_{Bri} \times V_{Bri} + \rho \times A_{Clay} \times V_{Clay} + \rho \times A_{TOC} \times V_{TOC} \quad (2)$$

In Equation (1), φ_{Total} is the total shale porosity; φ_{Matrix} is the shale matrix porosity; φ_{Frac} is the shale fracture porosity, which is calculated by $\varphi_{Total} - \varphi_{Matrix}$, while Equation (2) is the shale matrix porosity, ρ is the shale rock density ($t \cdot m^{-3}$), A is the percent mineral content (%), and V is the pore volume per unit mass of each rock ($t \cdot m^{-3}$).

2.2.3. Basic Geochemical and Mineral Properties

In the logging laboratory of CNPC Logging Co., Ltd., the samples were tested using a CS230HC carbon-sulfur analyzer. The sample was crushed to 200-mesh powder and then treated with dilute hydrochloric acid to remove the carbonate, as per the national standard GB/T19145-2003 [30]. The samples were then burned in a high-frequency induction furnace to cause the organic matter to burn and release CO_2 , and the TOC concentration was measured using infrared spectroscopy. The AXS X-ray diffractometer (D8 ADVANCE, Bruker, Billerica, MA, USA) test process was based on the industry standard SY/T5163-2010 [31]. Firstly, the sample was ground to 200 mesh powder, the ambient temperature was maintained at 20 °C, and the humidity was 70%. The mineral composition and content

of shale were determined by using the standard powder diffraction analysis data (Data Center of the Federation). The relative uncertainty of the test was less than 5%.

This study used the J & M MSP200 microspectrophotometry system, oil immersion lens, and photometer to measure the R_b value on thin slices, and this experiment was performed at the Natural Gas Research Institute. The equivalent vitrinite reflectance (R_{oeq}) is calculated by R_b , due to the lack of vitrinite macerals in the Ordovician Silurian strata. The empirical formula $R_{oeq} = (R_b + 0.2443)/1.0495$ was used for calculation [32].

3. Results

3.1. Mineralogy and Organic Petrography

The shale samples had a total organic carbon content (TOC) of 0.7% to 6.1%, with an average of 3.0%, and were organic-rich shales; the TOC concentration rose with depth. R_O (vitrinite reflectivity) content ranged from 2.91% to 3.41%, with a 3.14% average. Brittle mineral content ranges from 34.5% to 70.1% (mean 50.2%) and is primarily made of quartz (20.1 wt% to 51.1 wt%, mean 35.4 wt%). The clay mineral composition ranged from 11.2 to 49.3 weight percent, with an average of 31.5 weight percent. Other minerals, such as pyrite and rhodochrosite, are also present, with concentrations of less than 5%. (Table 1). Through the analysis of box plot (Figure 3) and Shapiro–Wilk (SW) test (Table A1), it is considered that the mineral test results of the selected samples do not have extreme abnormal values, and have good homogeneity and linearity. All the mineral tests of the selected samples are effective.

Table 1. TOC content and mineralogical composition of Wufeng–Longmaxi shale samples.

| Sample | Depth (m) | TOC (%) | R_O (%) | Quartz (wt%) | Dolomite (wt%) | Pyrite (wt%) | Feldspar (wt%) | Calcite (wt%) | Brittle min (wt%) | Clay min (wt%) |
|----------|-----------|---------|-----------|--------------|----------------|--------------|----------------|---------------|-------------------|----------------|
| Y108-L1 | 2382.43 | 0.7 | 2.91 | 20.1 | 7.4 | 0.5 | 5.5 | 23.4 | 34.5 | 36.7 |
| Y108-L2 | 2386.75 | 1.1 | 2.82 | 29.9 | 6.7 | 0.8 | 7.1 | 17.6 | 44 | 31.2 |
| Y108-L3 | 2467.47 | 1.3 | 2.96 | 32.1 | 2.2 | 1.2 | 8.1 | 4.7 | 38 | 49.3 |
| Y108-L4 | 2472.93 | 1.2 | 3.02 | 42.5 | 3 | 0.9 | 10.3 | 7.9 | 48 | 33.8 |
| Y108-L5 | 2477.91 | 1.0 | 3.02 | 31.7 | 18.1 | 2 | 8.2 | 10.7 | 51.8 | 29.3 |
| Y108-L6 | 2485.48 | 2.6 | 3.11 | 44 | 2.2 | 1.3 | 5.2 | 5.7 | 47.5 | 41.5 |
| Y108-L7 | 2490.28 | 2.9 | 3.07 | 43.9 | 1.1 | 1.8 | 4.1 | 4.6 | 46.8 | 44.5 |
| Y108-L8 | 2494.15 | 2.5 | 3.06 | 44 | 0.7 | 2 | 4.6 | 3.8 | 46.7 | 44.9 |
| Y108-L9 | 2500.3 | 4.5 | 3.16 | 32.1 | 14.5 | 1.9 | 4.3 | 8.3 | 61 | 26.3 |
| Y108-L10 | 2504.09 | 4.5 | 3.30 | 37.8 | 8.4 | 1.6 | 5.7 | 16.7 | 54 | 23.5 |
| Y108-L11 | 2507.67 | 3.7 | 3.34 | 51.1 | 9.8 | 2.3 | 3 | 15.7 | 70.1 | 11.2 |
| Y108-L12 | 2509.5 | 3.4 | 3.33 | 47.9 | 8.6 | 1.5 | 4.1 | 12.1 | 58 | 25.8 |
| Y108-W13 | 2510.38 | 6.1 | 3.35 | 26.1 | 12.7 | 2.2 | 3.3 | 13.9 | 53.4 | 29.3 |
| Y108-W14 | 2511.69 | 5.1 | 3.28 | 18.5 | 19 | 2.2 | 3.4 | 27.5 | 52.1 | 17 |
| Y108-W15 | 2512.15 | 5.1 | 3.41 | 29.4 | 9 | 1.2 | 3.8 | 20.8 | 47.6 | 27.8 |

3.2. FE-SEM Image Processing

Matrix pores and fractures are two types of pores found in shale. Mineral grain intergranular pores, mineral grain intragranular pores, and organic matter pores are the three types of matrix pores [33]. In FE-SEM pictures of the Longmaxi Formation shale in the Zhaotong area, all these pore types and microfractures can be observed (Figure 4). Clay minerals, quartz grains, carbonate grains, pyrite, and organic materials comprise the mineral framework. Intergranular pores are irregular in shape and typically exist between clay mineral skeletons, within pyrite grains, between clay and mineral grains, or between stiff grains, and are mostly associated with the retention of primary porosity but may also be related to diagenesis (Figure 4B,D,F). Within the particles are intra-granular pores, which are more abundant in neighboring layered clay minerals. Moreover, intra-granular holes are commonly generated within particles due to dissolution or late diagenesis (Figure 4A,D). Organic matter pores are abundant in samples with rounded or elliptical nanopores (Figure 4C,E), while some organic matter has no holes (Figure 4F), which could be attributed to different forms of organic matter. Fractures can be seen within the fractures of lamellar clay minerals, and a few microfractures can be found at the interface between organic matter and mineral grains, with serrated or uneven edges, or serrated at the edges of brittle minerals (Figure 4B,E).

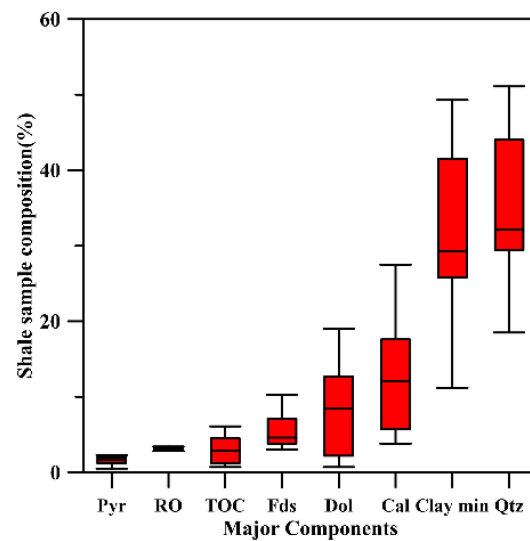


Figure 3. Effectiveness analysis diagram of mineral component test results.

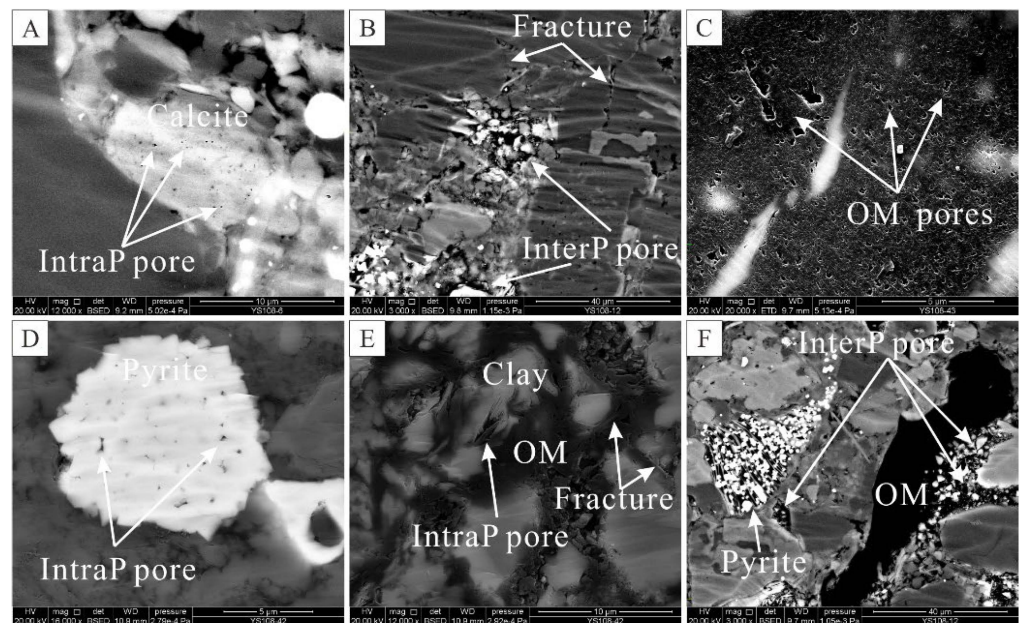


Figure 4. FE-SEM images of Wufeng-Longmaxi Fm shale within typical pore types. (A) Intraparticle pore of calcite; (B) Mineral grains interparticle pores and fracture; (C) Organic matter pores; (D) Intraparticle pore of pyrite; (E) Clay minerals interparticle pore and fracture; (F) Brittle mineral interparticle pore. OM—Organic Matter.

3.3. Calibration Calculation and Verification of Key Parameters

V_{Bri} , V_{Clay} , and V_{TOC} are three substances that contribute to porosity per unit mass. They are important model parameters that must be generated by picking data points in the evaluation area without fractures for scaled computations. Three samples (Y108-L2, Y108-L7, and Y108-L10) were randomly chosen for this study (Table 2) and we used equations to create a ternary linear system of equations for TOC, mineral content, porosity, and rock density [28]. Solving the system of equations yielded V_{Bri} , V_{Clay} , and V_{TOC} values of 0.0073, 0.0137, and 0.337 m^3/t , respectively. The V_{Bri} and V_{Clay} values in this result were like those of the Longmaxi Formation shale in the Changning and Fuling gas fields, while the V_{TOC} was significantly higher than the latter two (Table 3) [29]. The porosity of all samples, including matrix and fracture porosity, was determined using the results of the above three primary parameters (V_{Bri} , V_{Clay} , and V_{TOC}) (Figures 5 and 6). The computed

matrix porosity (2.4% to 6.7%, with an average value of 4.5%) was compared to the porosity measured by HMIP (3.2% to 6.4%, with an average value of 5.2%) in this study to illustrate the dependability and validity of the three essential parameters (Figure 5B). The results of the comparison indicated that the matrix porosity calculated from the 15 samples and the porosity obtained from the tests were in good agreement, which is consistent with the actual geological background of the Wufeng-Longmaxi Formation shale reservoir in the Zhaotong area and can be used as an effective means of studying the calculation and characterization of matrix porosity in the Zhaotong area.

Table 2. Sampling point parameters in the Wufeng–Longmaxi Formation.

| Sample | Depth (m) | Basic Data | | | | Micropore Volume Per Unit Mass (m ³ /t) | | | |
|----------|-----------|-----------------|--------------|---------|--------------|--|------------------|-------------------|------------------|
| | | Brittle Min (%) | Clay Min (%) | TOC (%) | Porosity (%) | Density (g/cm ³) | V _{Bri} | V _{Clay} | V _{TOC} |
| Y108-L3 | 2467.47 | 34.5 | 36.7 | 0.7 | 3.2 | 2.66 | 0.0133 | 0.0074 | 0.26 |
| Y108-L4 | 2472.93 | 61 | 26.3 | 4.5 | 5.7 | 2.65 | | | |
| Y108-L11 | 2507.67 | 52.1 | 17 | 5.1 | 6.3 | 2.67 | | | |

Table 3. Comparison of reservoir parameters between Wufeng–Longmaxi Formation shale in Zhaotong Area and other areas.

| Area | Brittle Min (%) | Clay Min (%) | TOC (%) | V _{Bri} | V _{Clay} | V _{TOC} | Calculate Matrix Porosity (%) |
|-----------|-------------------|-------------------|----------------|------------------|-------------------|------------------|-------------------------------|
| Zhaotong | 47.1~79.6 61.9 | 17~49.3 31.5 | 0.7~6.1 3 | 0.0133 | 0.0074 | 0.26 | 2.4~6.7 4.5 |
| Changning | 38.4~90.4 68.6 | 8.0~52.8 29.3 | 1.9~5.4 3.6 | 0.0079 | 0.039 | 0.138 | 3.4~8.4 5.5 |
| Fuling | 50.9~79.9 64.9 | 19.8~49.3 34.4 | 2.3~4.7 3.6 | 0.0061 | 0.025 | 0.169 | 4.6~7.8 6.1 |

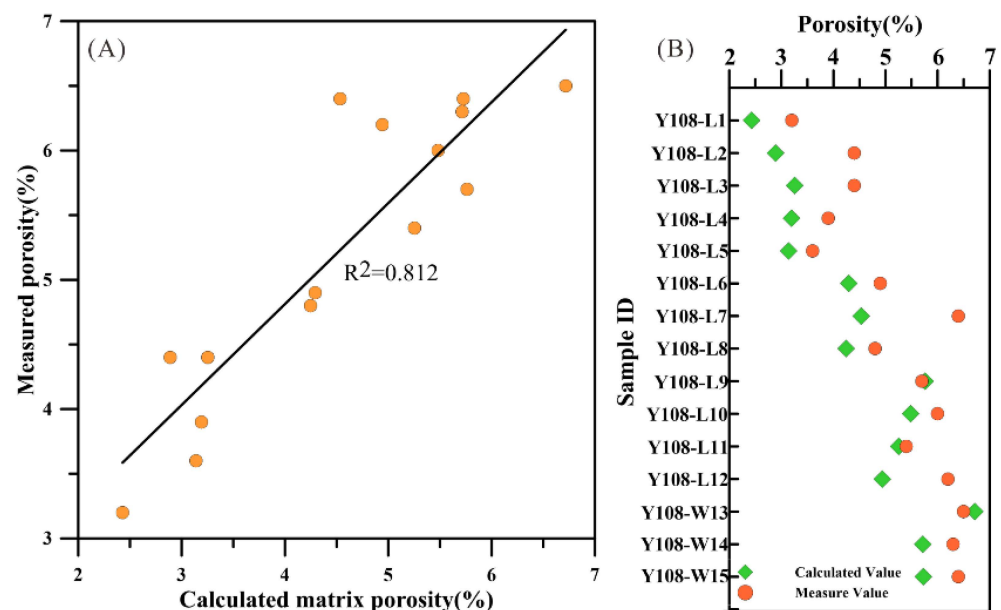


Figure 5. Correlation of the calculated and measured porosity of Wufeng–Longmaxi shale samples. (A) Figure of correlation between calculated matrix porosity and measured porosity; (B) Comparison of calculated matrix porosity and measured porosity.

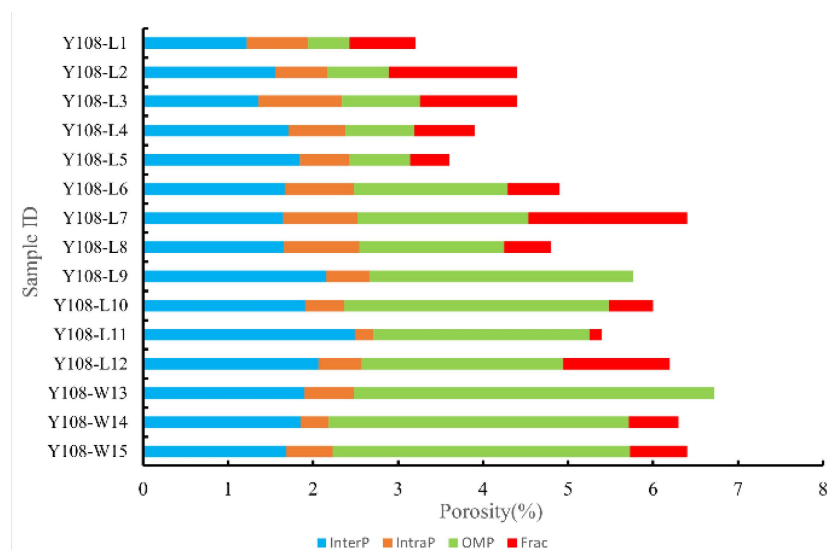


Figure 6. Total porosity constitution of the Wufeng–Longmaxi Fm shale samples. InterP—interparticle pores; IntraP—Intraparticle pore; OMP—Organic matter pores; Frac—fracture.

According to calculations, matrix porosity ranges from 3.06% to 7.67% (mean: 5.08%), while fracture porosity ranges from 0 to 1.14% (mean: 0.29%) (Figure 5) organic matter (OM) porosity ranged from 0.63% to 4.58% (average: 2.73%) in the matrix porosity composition, while brittle mineral intergranular porosity ranged from 0.92% to 1.55% (average: 1.2%) and clay mineral intragranular porosity ranged from 0.41% to 1.82% (average: 1.15%). OM porosity increased with depth; however, the influence of depth on mineral and fracture porosity was negligible (Figure 5).

3.4. Low-Pressure Gas Adsorption and HMIP

3.4.1. N₂ and CO₂ Adsorption Isotherms

Adsorption isotherms are divided into five types (types I–VI), hysteresis gyrus is divided into four types (types H1–H4), and pore fractures are divided into micropores (less than 2 nm in diameter), mesopores (2 nm to 50 nm), and macropores (more than 50 nm in diameter) by the International Union of Pure and Applied Chemistry (IUPAC) [33,34].

The N₂ adsorption isotherm type of the Wufeng–Longmaxi Formation shale is type IV, the hysteresis loop type is H3–H4 (Figure 7A–C), and the CO₂ adsorption isotherm type is type I, according to the aforementioned categorization standards (Figure 7D–F). The presence of mesoporous and macroporous porous media in the shale samples is indicated by the type II adsorption isotherm. The pore morphology in the Wufeng–Longmaxi Formation shales is primarily slit-like pores and wedge-shaped pores, as indicated by the H3–H4 hysteresis return type. Furthermore, according to data on N₂ adsorption volume, the mesopores of Longtan shale expand as the TOC concentration rises (Figure 7A–C).

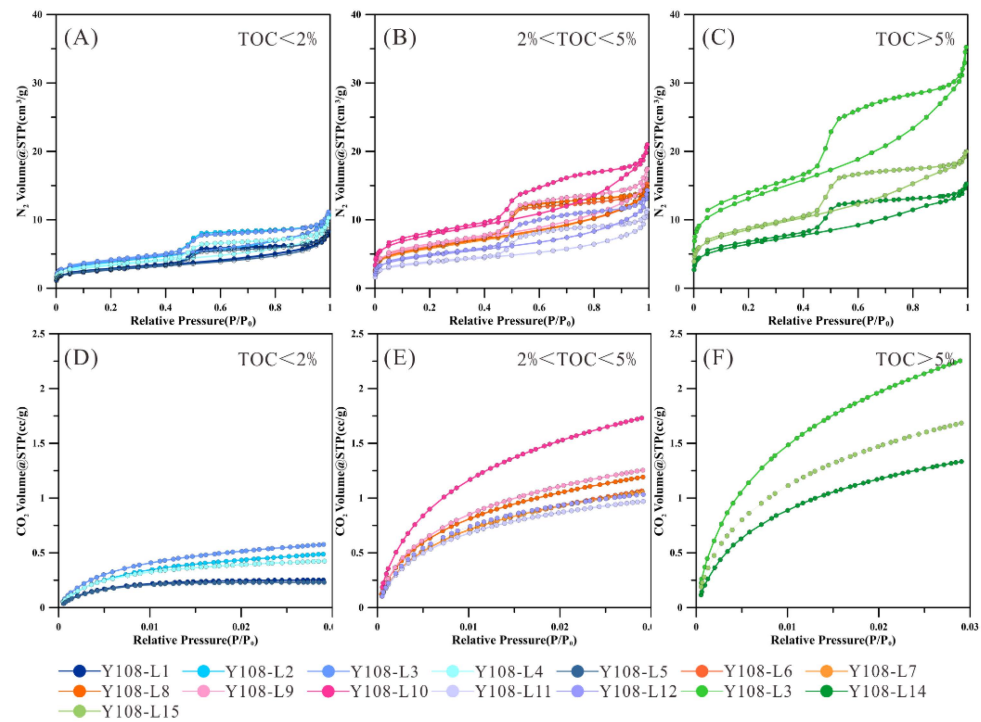


Figure 7. Low-pressure N₂ and CO₂ adsorption isotherms of Wufeng-Longmaxi formation shales. (A) N₂ adsorption-desorption curve with TOC < 2%; (B) N₂ adsorption-desorption curve with 2% < TOC < 5%; (C) N₂ adsorption-desorption curve with TOC > 5%; (D) CO₂ adsorption-desorption curve with TOC < 2%; (E) CO₂ adsorption-desorption curve with 2% < TOC < 5%; (F) CO₂ adsorption-desorption curve with TOC > 5%.

3.4.2. Pore Structure Parameters

The PV and SSA results obtained from the high-pressure mercury injection and low-pressure N₂/CO₂ adsorption tests of the selected shale samples were analyzed by box plot (Figure 8) and Shapiro-Wilk (SW) test (Table A2). There was no extreme abnormal value, and there was a certain homogeneity and linearity, so the test results were effective.

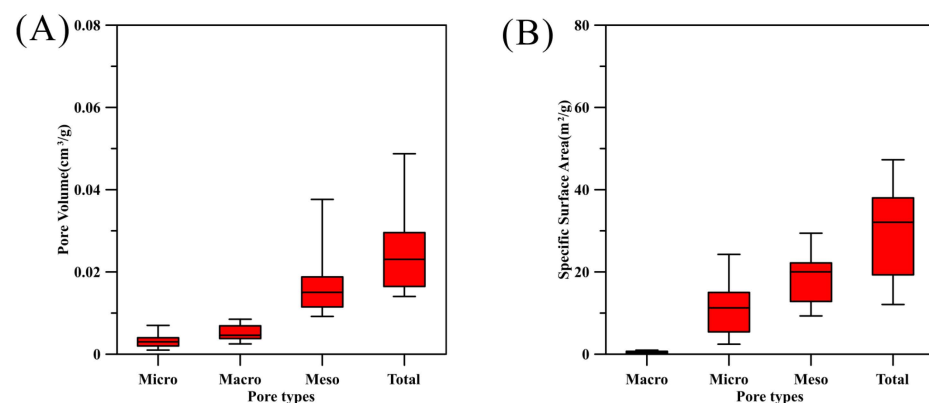


Figure 8. Validity analysis of PV (A) and SSA (B) data for different types of pores.

Quantitative characterization of PV and SSA is an important aspect of reservoir evaluation and can be utilized to delve deeper into the shale gas reservoir region. Based on different pore models and adsorption theories, the results from HMIP and low-pressure gas adsorption experiments can be used to calculate pore structure characteristics [29]. The BET model was used to calculate SSA from N₂ adsorption data, and the BJH model was utilized to calculate PV for mesopores and macropores in this study. The DFT model based on CO₂

adsorption data was used to produce microporous SSA and PV. The PV and SSA of the samples were 0.016–0.049 cm³/g (mean: 0.024 cm³/g) and 12.1–69.8 m²/g (mean: 31 m²/g), respectively, as indicated in Table 3. Micropores had pore volumes of 0.003–0.007 (mean: 0.003 cm³/g) and mesopores had pore values of 0.009–0.020 cm³/g (mean: 0.016 cm³/g), respectively. Micropores had an SSA of 2.6–18.3 m²/g (average: 11 m²/g) and mesopores had an SSA of 9.31–45.3 m²/g (average: 19.5 m²/g), respectively. Pore sizes ranged from 4.04 nm to 5.19 nm on average (average: 4.61 nm). Micropores and mesopores comprise 78% of total pore volume and 98 percent of total specific surface area, making them crucial in shale gas transfer.

MIP and N₂/CO₂ adsorption data can be used to determine the PSD (pore size distribution characteristics). Previous research has discovered that, due to differences in testing methods, molecule sizes, and other factors, the three procedures have distinct principal measurement coverage. Given the foregoing, MIP analysis is used to evaluate the pore size distribution of big pores or fractures (>50 nm); N₂ adsorption is used to define the pore size distribution of mesopores, and CO₂ adsorption is used to characterize the pore size distribution of micropores. Figure 9A displays the pore size distribution (PSD) of large pores exhibited by the 15 tested shale samples in the MIP test analysis, with pore sizes ranging from 5 nm to 10 μm and 2 primary peaks in the pore size distribution, 5–20 nm and around 1000 nm, where the larger portion (5–20 nm) represents the nanopore system and the smaller portion (>1000 nm) represents the pore microfracture system. Figure 9B illustrates the analysis of the mesopore pore size distribution (PSD) characterized by N₂ adsorption, which reveals that the pore size distribution of the shale has two peaks, about 1–2 nm and 3–5 nm. The micropore pore size distribution (PSD) of the examined shale samples is provided in Figure 9C, which reveals that the shale's micropore pore size range is 0.30–0.8 nm, with several peaks at 0.35 nm, 0.45 nm, and 0.8 nm, indicating that the micropore distribution of these three pore sizes is greater.

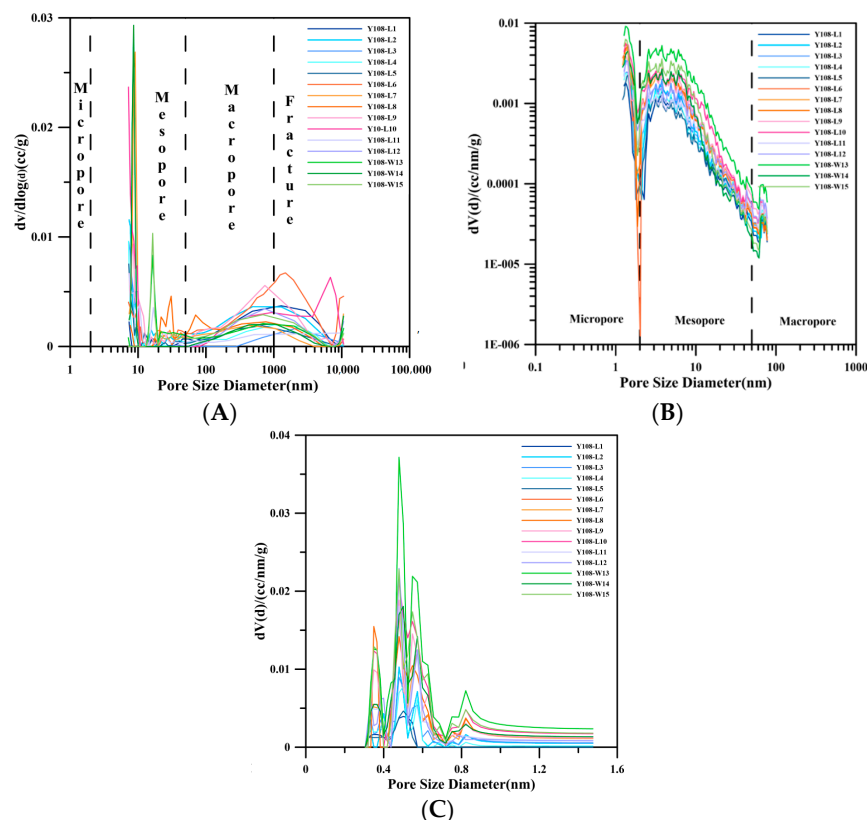


Figure 9. Pore Size Distribution (PSD) explained by MIP and N₂ and CO₂ adsorption. (A) The pore structure distribution curve of HMIP; (B) The pore structure distribution curve of low-temperature N₂ adsorption; (C) The pore structure distribution curve of low-temperature CO₂ adsorption.

3.5. Diagenetic Evolution

The Ro values of the Wufeng–Longmaxi Formation shales in the Zhaotong area range from 2.91 to 3.68% (average 3.14%), indicating that the reservoir shales have reached an advanced stage of dry gas generation. The compaction, cementation, and dissolution were discovered as the key diagenetic events when combined with scanning electron microscope observations. Furthermore, the thermal maturation of organic matter is a type of diagenesis [35].

3.5.1. Mechanical Compaction

Compaction is an irreversible process of rock formation that reduces porosity [36]. In the Wufeng–Longmaxi shale, compaction manifests itself predominantly as surface fractures on stiff particles (Figure 10A), ductile particle deformation (Figure 10B), and particle semi-direction (Figure 10C).

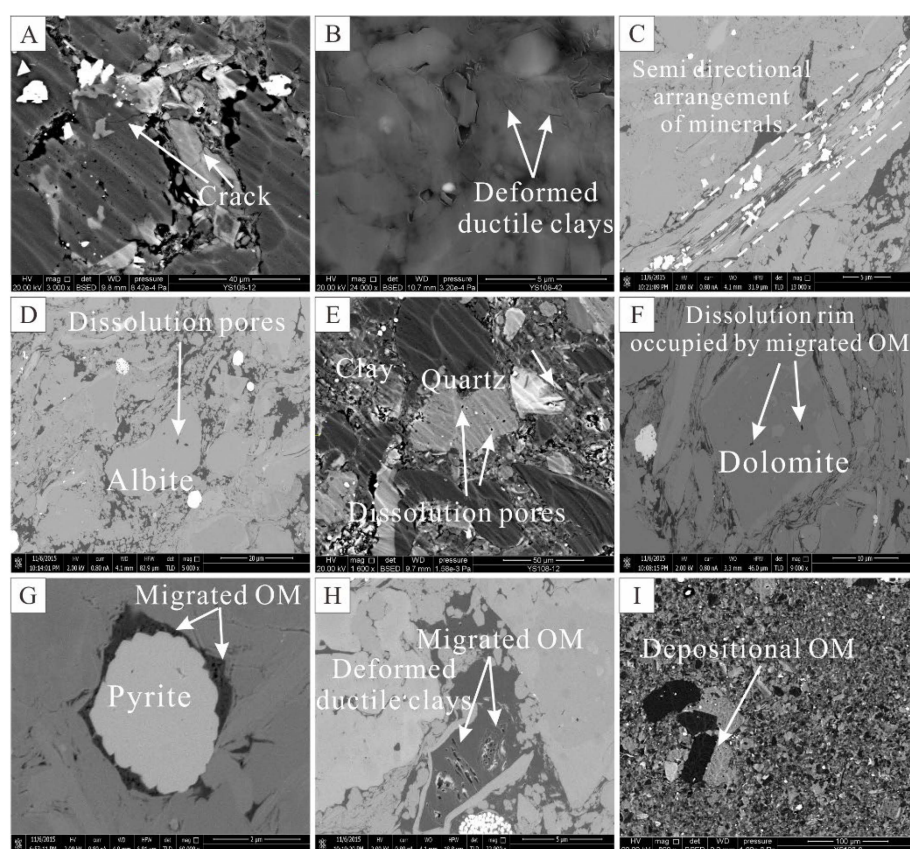


Figure 10. FE-SEM images of Wufeng-Longmaxi Fm shale within pore types formed during diagenetic evolution. (A) Cracks formed under mechanical compaction; (B) The ductile deformation of clay minerals under mechanical compaction; (C) Directional arrangement of minerals under mechanical compaction; (D) Dissolution pores in albite under dissolution; (E) Dissolution pores in quartz under dissolution; (F) Dissolution pores in dolomite under dissolution; (G) Organic matter pores in migrating organic matter; (H) The ductile deformation of clay minerals under mechanical compaction and organic matter pores; (I) Depositional organic matter pores.

3.5.2. Dissolution

The diagenesis that can lead to the increase of pore space is primarily dissolution. This interaction occurs widely among quartz, feldspar, calcite, and dolomite grains, with sodium feldspar being more susceptible to dissolution (Figure 10D). The difference between the dissolution of different minerals is that the dissolution holes of dolomite and quartz are often hollow oval or round holes, while the dissolution holes of feldspar and calcite are always filled with migrating OM (Figure 10E,F). This indicates that dissolution occurs at different

times for different minerals. Figure 8 depicts the order of mineral dissolution: feldspar and calcite dissolution, massive asphalt formation, and quartz and dolomite dissolution.

3.5.3. Thermal Maturation of OM

During the diagenetic evolution of organic-rich shales, organic matter undergoes burial thermomaturation. Organic matter is changed from kerogen to petroleum and then from petroleum to dry-formed gas in this process, which also produces some intermediate products like bitumen [37]. The kerogen creates asphalt, which migrates to the nearby pore space. Organic matter pores are mostly concentrated in migrating organic matter, according to prior investigations [38]. Because of its higher thermal maturity, the Longmaxi shale of Wufeng has spongy organic matter pores in practically all migrating organic matter (Figure 10G,H). The sedimentary OM has no pore formation observable at the SEM observation scale (Figure 10I). Internal pore space will be created during the thermal transformation of sedimentary organic materials to petroleum. As soluble minerals dissolve in Porewater which is rich in organic acids, the OM dissolution process produces alteration products, and the mineral matrix reacts with these alteration products. Furthermore, the presence of moving organic matter in the pore space may raise internal pore pressure, reducing the compaction impact to a degree.

4. Discussion

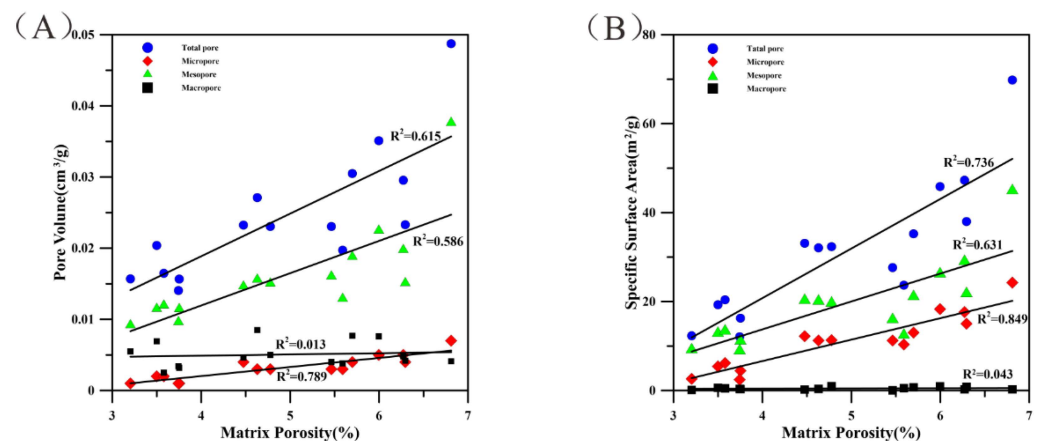
4.1. Full-Scale Pore-Fracture Distribution Characteristics of Shale

According to the calculation of the dual-pore petrophysical model, two types of pores—matrix pores and microfractures—exist in the shales of the region of interest. In the matrix pores, organic matter pores dominate, followed by intra- and inter-grain pores ($V_{\text{TOC}} > V_{\text{Bri}} > V_{\text{Clay}}$), with microfractures only developed in some shale samples. Combined with FE-SEM images, it was discovered that the matrix pores contain different types of pores, such as intergranular pores supported by brittle minerals such as quartz, dissolution pores formed by carbonate minerals such as calcite during diagenesis, intercrystalline pores within clay minerals, and intergranular pores between clay minerals.

The multi-scale pore characterization by combined high-pressure mercury pressure and N_2/CO_2 adsorption (Figure 7) demonstrated that the pore size distribution of MIP was primarily bimodal, with the primary peak pore size around 10 nm, primarily representing organic matter pores and matrix pores; the secondary peak pore size was around 1000 nm, primarily representing the microfracture-dominated pore type. Of the three pore types, the contribution of micropores and mesopores to the pore volume was the largest, comprising up to 78%, and the contribution of macropores to the pore volume was the smallest (Table 4). The link between matrix porosity and pore volume, SSA, average pore size, and surface porosity was explored (Figure 11), and a phenomenon was discovered that with increasing matrix porosity, both pore volume and SSA increased in a positive linear relationship. However, different pore sizes have varied linear fit strengths: micropores have the strongest association, followed by mesopores, and then macropores (Figure 11A). These findings imply that micropores and mesopores are the primary pores in the Wufeng–Longmaxi Formation shale reservoir in the Zhaotong area. Furthermore, micropores and mesopores have a substantially greater specific surface area than macropores (Figure 11B), indicating that micropores and mesopores are the major adsorption sites in the Wufeng–Longmaxi Formation shales.

Table 4. Pore volumes and SSAs of Wufeng–Longmaxi Fm shales depend on MIP and N₂/CO₂ isotherms.

| Sample | Pore Volume(cm ³ /g) | | | | Specific Surface Area(m ² /g) | | | | Average Pore Diameter(nm) |
|----------|---------------------------------|----------|-----------|-------|--|----------|-----------|--------|---------------------------|
| | Macropore | Mesopore | Micropore | Total | Macropore | Mesopore | Micropore | Total | |
| Y108-L1 | 0.0055 | 0.009182 | 0.001 | 0.016 | 0.140 | 9.548 | 2.622 | 12.310 | 4.972 |
| Y108-L2 | 0.0069 | 0.01149 | 0.002 | 0.020 | 0.620 | 13.250 | 5.425 | 19.295 | 4.683 |
| Y108-L3 | 0.0025 | 0.01197 | 0.002 | 0.016 | 0.480 | 13.750 | 6.176 | 20.406 | 4.661 |
| Y108-L4 | 0.0032 | 0.01147 | 0.001 | 0.016 | 0.290 | 11.500 | 4.455 | 16.245 | 4.99 |
| Y108-L5 | 0.0034 | 0.009638 | 0.001 | 0.014 | 0.350 | 9.305 | 2.428 | 12.083 | 5.189 |
| Y108-L6 | 0.0085 | 0.01561 | 0.003 | 0.027 | 0.360 | 20.470 | 11.243 | 32.073 | 4.358 |
| Y108-L7 | 0.005 | 0.01504 | 0.003 | 0.023 | 0.980 | 20.030 | 11.324 | 32.334 | 4.401 |
| Y108-L8 | 0.0046 | 0.01463 | 0.004 | 0.023 | 0.230 | 20.670 | 12.214 | 33.114 | 4.228 |
| Y108-L9 | 0.0077 | 0.01879 | 0.004 | 0.030 | 0.700 | 21.520 | 13.006 | 35.226 | 4.559 |
| Y108-L10 | 0.0076 | 0.0225 | 0.005 | 0.035 | 0.940 | 26.600 | 18.317 | 45.857 | 4.604 |
| Y108-L11 | 0.0038 | 0.01291 | 0.003 | 0.020 | 0.510 | 12.820 | 10.356 | 23.686 | 5.016 |
| Y108-L12 | 0.004 | 0.01606 | 0.003 | 0.023 | 0.060 | 16.340 | 11.253 | 27.653 | 4.948 |
| Y108-W13 | 0.0041 | 0.03764 | 0.007 | 0.049 | 0.260 | 45.300 | 24.267 | 69.827 | 4.497 |
| Y108-W14 | 0.0042 | 0.01511 | 0.004 | 0.023 | 0.800 | 22.190 | 15.016 | 38.006 | 4.072 |
| Y108-W15 | 0.0048 | 0.01976 | 0.005 | 0.030 | 0.240 | 29.420 | 17.616 | 47.276 | 4.042 |

**Figure 11.** Correlation among the matrix porosity, PV, and SSA of Wufeng–Longmaxi shales. (A) Correlation between matrix porosity and pore volume; (B) Correlation between matrix porosity and specific surface area.

4.2. Primary Controlling Factors of Pores

4.2.1. Composition Controls Pores

The impacts of TOC, brittle minerals, and clay minerals on pore space were studied by the authors. This publication displayed the association between TOC content and porosity, pore volume, and specific surface area in this investigation (Figure 12A–C). Figure 12A indicates that the pore fracture system (PFS) of the Wufeng–Longmaxi Formation shale has a good relationship between TOC and porosity ($R^2 = 0.88$), suggesting that TOC plays an extremely beneficial role in the PFS of the Wufeng–Longmaxi Formation shale. TOC content has a substantial positive connection with micropore and mesopore-specific surface area and pore volume, but not with macropores. TOC content is crucial in the storage and enrichment of shale gas, as indicated in the correlation plots between TOC and the specific surface area and pore volume of different pore sizes (Figure 12B,C). $R^2 = 0.29$ of porosity has a weak positive connection with brittle minerals (Figure 12D). Also, for pore structure characteristics (Figure 12E,F), there is a modest positive connection between the specific surface area of brittle minerals and micropores ($R^2 = 0.18$, $R^2 = 0.13$), indicating that brittle minerals have a role in shale pores, particularly micropores. Clay minerals contribute less to shale matrix porosity ($R^2 = 0.13$, negative correlation) than the first two (Figure 12G) and do not play a bigger role in pore structure determination (Figure 12H,I). The result

here indirectly illustrates the validity of the essential parameters V_{Bri} , V_{Clay} , and V_{TOC} determined from the dual-porosity physical model in the previous study.

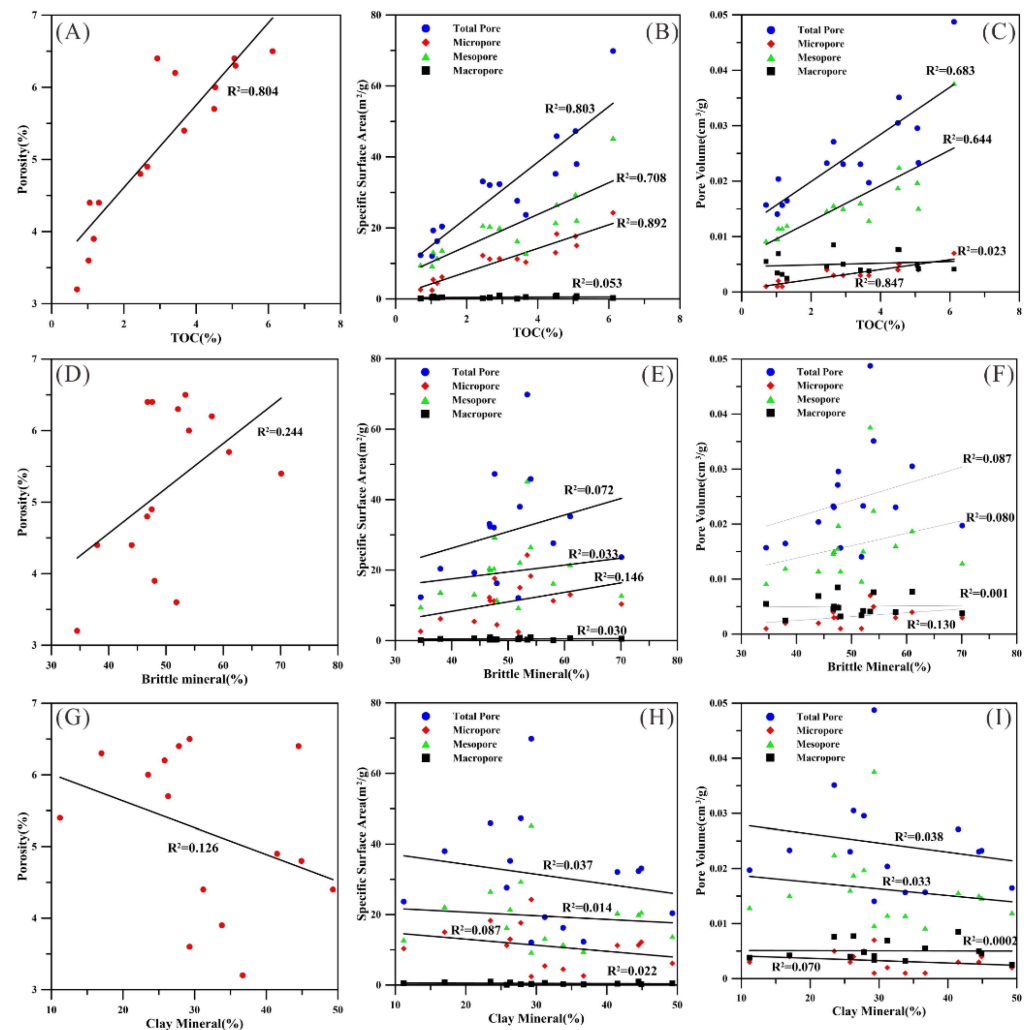


Figure 12. Relationship diagram of pore structure with mineral and TOC in Wufeng–Longmaxi Fm of Y108. (A) Correlation between TOC and porosity; (B) Correlation between TOC and specific surface area of different types of pores; (C) Correlation between TOC and pore volume of different types of pores; (D) Correlation between Brittle mineral and porosity; (E) Correlation between Brittle mineral and specific surface area of different types of pores; (F) Correlation between Brittle mineral and pore volume of different types of pores; (G) Correlation between Clay mineral and porosity; (H) Correlation between Clay mineral and specific surface area of different types of pores; (I) Correlation between Clay mineral and pore volume of different types of pores.

4.2.2. Organic–Inorganic Diagenesis Evolution on Pores

The complete effect of diagenesis of the shale during burial plays a significant role in the creation of pore space, in addition to the most fundamental influence of minerals and organic matter on the shale pore fracture system. Various diageneses, such as compaction, dissolution, and thermal evolution of organic matter were observed in the process of scanning electron microscopy. This indicates that the Wufeng–Longmaxi Formation shales in the Zhaotong area have undergone many stages of diagenesis, based on prior studies on the thermal history of the Wufeng–Longmaxi Formation shales in other locations of the Sichuan Basin [39]. Rigid minerals such as early authigenic pyrite, biotite, and microbial dolomite are typically dispersed as microcrystalline and microcrystalline aggregates along the perimeter of land-derived grains, or fill the original intergranular gaps when mechanical and compaction are weak (Figure 10A,B). These rigid minerals are both helpful and

harmful in maintaining the shale's natural pore space [40]. The middle diagenetic phase began with the progressive increase in burial depth compaction. The disintegration of unstable minerals like feldspar and carbonate formed additional secondary pores due to the production of organic acids (Figure 10D–F). The increase of pore pressure and the development of secondary pores constitute a favorable combination of pores and fractures, which provides a favorable space for the filling and retention of liquid hydrocarbon during oil generation [41]. When entering the late diagenetic stage, kerogen, retained hydrocarbon cracked gas, pore-forming, and pressurization promoted the development of organic pores and micro-fractures (Figure 10G,H), which was conducive to the enrichment and high yield of late shale gas.

In this paper, the relationship between vitrinite reflectance (R_o) and porosity is discussed. It is discovered that there is a strong positive correlation between porosity and vitrinite reflectance ($R^2 = 0.638$) (Figure 13A). This indicates that in the thermal evolution process of organic matter, with the deepening of thermal evolution, porosity will continue to increase. In the discussion of the correlation between R_o and SSA, it is discovered that R_o has a strong correlation with SSA ($R^2 = 0.626$, $R^2 = 0.397$) and PV ($R^2 = 0.546$, $R^2 = 0.386$) of micropores and mesopores. However, there is no correlation between SSA and PV of macropores (Figure 13B,C). This indicates that the thermal evolution of organic matter has a good control effect on the formation of micropores and mesopores.

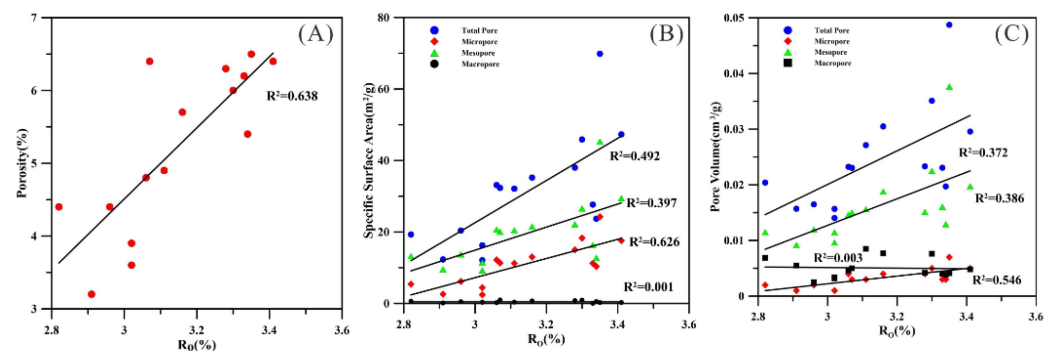


Figure 13. Relationship between pore structure and R_o in Wufeng–Longmaxi Fm of Y108. (A) Correlation between R_o and porosity; (B) Correlation between R_o and specific surface area of different types of pores; (C) Correlation between R_o and pore volume of different types of pores.

Overall, the development of pore-fracture system (PFS) in shale reservoirs is affected by multiple geological factors, such as mineral composition and diagenesis. Mineral pores include not only the original pores formed in the initial accumulation, but also various secondary pores formed in the process of diagenesis. In addition, the organic matter pores not only contain the original pores formed by the original accumulation of organic matter, but also many secondary organic matter pores formed during the thermal and diagenetic evolution.

5. Conclusions

This paper employed FE-SEM as a visualization tool to define pore types and undertake a qualitative analysis of pore morphology. The study also created a pore-fracture interpretation model to describe different types of pores and fractures quantitatively. To evaluate the pore structure quantitatively, the study process employed MIP and low-pressure N_2/CO_2 adsorption. Some conclusions have been reached based on the findings of this investigation.

- (1) The Wufeng–Longmaxi Formation shale pore types are varied and morphologically complex. Organic matter pores, dissolution pores, intergranular pores, intragranular pores, microfractures, and other types of pores are developed.

- (2) A model for interpreting pore fractures was created. The three major factors discovered were proven to be efficient in calculating and characterizing matrix pores. Organic pores predominate among matrix pores, followed by intergranular pores of brittle minerals, and clay minerals have the fewest intragranular pores ($V_{\text{TOC}} > V_{\text{Bri}} > V_{\text{Clay}}$).
- (3) High-pressure mercury intrusion and low-temperature gas adsorption tests conclude that micropores and mesopores are the primary pores in the shale gas reservoir of the Wufeng–Longmaxi Formation in the region of interest, providing the main space for the shale gas adsorption.
- (4) The pores of shale gas reservoirs in the Wufeng–Longmaxi Formation are primarily influenced by the OM content. The influence of brittle minerals on reservoir pore space is small. The clay minerals do not affect the pore space of shale. Additionally, because the shales of the Wufeng–Longmaxi Formation have entered the late diagenetic stage, the pore space is also influenced by the comprehensive influence of organic–inorganic synergistic diagenesis.

Author Contributions: Conceptualization, K.M., B.Z. and S.W.; methodology, K.M.; software, X.L.; validation, K.M., B.Z. and K.Y.; formal analysis, Y.W.; investigation, K.M.; resources, B.Z.; data curation, K.Y.; writing—original draft preparation, K.M. and S.W.; writing—review and editing, K.M. and S.W.; visualization, Y.W. and X.L.; supervision, B.Z.; project administration, B.Z.; funding acquisition, B.Z. All authors have read and agreed to the published version of the manuscript.

Funding: This work was supported by the National Natural Science Foundation of China (Grant No: 91755215).

Data Availability Statement: Not applicable.

Conflicts of Interest: The authors declare no conflict of interest.

Abbreviations

| Abbreviations | Full name |
|---------------|--------------------------|
| OM | Organic Matter |
| PFS | Pore and Fracture System |
| PSD | Pore Size Distribution |
| PV | Pore-Volume |
| Ro | Vitrinite Reflectivity |
| SSA | Specific Surface Area |
| TOC | Total Organic Carbon |

Appendix A

Homogeneity and linearity of the data in the results.

Table A1. Analysis of mineral composition data.

| Mineral Composition | Tests of Normality | | | | | |
|---------------------|---------------------|----|---------|--------------|----|-------|
| | Kolmogorov-Smirnova | | | Shapiro-Wilk | | |
| | Statistic | df | Sig. | Statistic | df | Sig. |
| TOC (%) | 0.172 | 15 | 0.200 * | 0.931 | 15 | 0.280 |
| Quartz (wt%) | 0.163 | 15 | 0.200 * | 0.949 | 15 | 0.512 |
| Dolomite (wt%) | 0.146 | 15 | 0.200 * | 0.929 | 15 | 0.264 |
| Pyrite (wt%) | 0.132 | 15 | 0.200 * | 0.945 | 15 | 0.454 |
| Feldspar (wt%) | 0.176 | 15 | 0.200 * | 0.889 | 15 | 0.065 |
| Calcite (wt%) | 0.134 | 15 | 0.200 * | 0.943 | 15 | 0.418 |
| Clay min (wt%) | 0.115 | 15 | 0.200 * | 0.973 | 15 | 0.902 |

* This is a lower bound of the true significance.

Table A2. Pore structure data analysis.

| Analysis of Pore Specific Surface Area Data | | | | | | |
|---|---------------------|----|---------|--------------|----|-------|
| Tests of Normality | | | | | | |
| Different types of pores SSA | Kolmogorov-Smirnova | | | Shapiro-Wilk | | |
| | Statistic | df | Sig. | Statistic | df | Sig. |
| Total SSA | 0.126 | 15 | 0.200 * | 0.923 | 15 | 0.213 |
| Micropore SSA | 0.122 | 15 | 0.200 * | 0.953 | 15 | 0.575 |
| Mesopore SSA | 0.187 | 15 | 0.165 | 0.867 | 15 | 0.030 |
| Macro pore SSA | 0.175 | 15 | 0.200 * | 0.936 | 15 | 0.335 |

| Analysis of pore volume data | | | | | | |
|------------------------------|---------------------|----|---------|--------------|----|-------|
| Tests of Normality | | | | | | |
| Different types of pores PV | Kolmogorov-Smirnova | | | Shapiro-Wilk | | |
| | Statistic | df | Sig. | Statistic | df | Sig. |
| Total PV | 0.213 | 15 | 0.064 | 0.879 | 15 | 0.045 |
| Micropore PV | 0.147 | 15 | 0.200 * | 0.934 | 15 | 0.318 |
| Mesopore PV | 0.237 | 15 | 0.023 | 0.778 | 15 | 0.002 |
| Macropore PV | 0.178 | 15 | 0.200 * | 0.918 | 15 | 0.178 |

* This is a lower bound of the true significance.

References

- Zou, C.; Zhao, Q.; Cong, L.; Wang, H.; Shi, Z.; Wu, J.; Pan, S. Development progress, potential and prospect of shale gas in China. *Nat. Gas Ind.* **2021**, *41*, 1–14.
- Liu, Z.; Qiu, H.; Jiang, Z.; Liu, R.; Wei, X.; Chen, F.; Wei, F.; Wang, D.; Su, Z.; Yang, Z. Types and Quantitative Characterization of Microfractures in the Continental Shale of the Da'anzhai Member of the Ziliujing Formation in Northeast Sichuan, China. *Minerals* **2021**, *11*, 870. [[CrossRef](#)]
- Zhang, D.; Dai, Y.; Ma, X.; Zhang, L.; Zhong, B.; Wu, J.; Tao, Z. An analysis for the influences of a fracture network system on multi-stage fractured horizontal well productivity in shale gas reservoirs. *Energies* **2018**, *11*, 414. [[CrossRef](#)]
- Mastalerz, M.; Schimmelmann, A.; Drobniak, A.; Chen, Y. Porosity of Devonian and Mississippian New Albany Shale across a maturation gradient: Insights from organic petrology, gas adsorption, and mercury intrusion. *AAPG Bull.* **2013**, *97*, 1621–1643. [[CrossRef](#)]
- Clarkson, C.; Haghshenas, B.; Ghanizadeh, A.; Qanbari, F.; Williams-Kovacs, J.; Riazi, N.; Debuhr, C.; Deglint, H. Nanopores to megafractures: Current challenges and methods for shale gas reservoir and hydraulic fracture characterization. *Nat. Gas Sci. Eng.* **2016**, *31*, 612–657. [[CrossRef](#)]
- Zhu, H.; Huang, C.; Ju, Y.; Bu, H.; Li, X.; Yang, M.; Chu, Q.; Feng, H.; Qiao, P.; Qi, Y.; et al. Multi-scale multi-dimensional characterization of clay-hosted pore networks of shale using FIBSEM, TEM, and X-ray micro-tomography: Implications for methane storage and migration. *Appl. Clay Sci.* **2021**, *213*, 106239. [[CrossRef](#)]
- Zhou, S.; Yan, G.; Xue, H.; Guo, W.; Li, X. 2D and 3D nanopore characterization of gas shale in Longmaxi formation based on FIB-SEM. *Mar. Pet. Geol.* **2016**, *73*, 174–180. [[CrossRef](#)]
- Tang, X.; Jiang, Z.; Jiang, S.; Li, Z. Heterogeneous nanoporosity of the Silurian Longmaxi Formation shale gas reservoir in the Sichuan Basin using the QEMSCAN, FIB-SEM, and nano-CT methods. *Mar. Pet. Geol.* **2016**, *78*, 99–109. [[CrossRef](#)]
- Garum, M.; Glover, P.W.J.; Lorinczi, P.; Drummond-Brydson, R.; Hassabpour, A. Micro- and nano-scale pore structure in gas shale using X μ -CT and FIB-SEM techniques. *Energy Fuels* **2020**, *34*, 12340–12353. [[CrossRef](#)]
- Clarkson, C.; Solano, N.; Bustin, R.; Bustin, A.; Chalmer, G.; He, L.; Melnichenko, Y.; Radliński, A.; Blach, T. Pore structure characterization of North American shale gas reservoirs using USANS/SANS, gas adsorption, and mercury intrusion. *Fuel* **2013**, *103*, 606–616. [[CrossRef](#)]
- Liang, X.; Zhang, C.; Shan, C.; Zhang, J.; Wang, W.; Xu, Z.; Li, Z.; Mei, J.; Zhang, L.; Xu, J.; et al. Exploration challenges, countermeasures and prospect of mountain shallow shale gas: A case study on the Zhaotong National Shale Gas Demonstration Area. *Nat. Gas Ind.* **2021**, *41*, 27–36.
- Zhang, J.; Shi, M.; Wang, D.; Tong, Z.; Hou, X.; Niu, J.; Li, X.; Li, Z.; Zhang, P.; Huang, Y. Fields and directions for shale gas exploration in China. *Nat. Gas Ind. B* **2022**, *9*, 20–32. [[CrossRef](#)]
- Liang, X.; Xu, Z.; Zhang, Z.; Wang, J.; Lu, H.; Zhang, L.; Zou, C.; Wang, G.; Mei, J.; Rui, I. Breakthrough of shallow shale gas exploration in Taiyang anticline area and its significance for resource development in Zhaotong, Yunnan province, China. *Pet. Explor. Dev.* **2020**, *47*, 11–28. [[CrossRef](#)]
- Liu, W.; Lu, L.; Wei, Z.; Yu, L.; Zhang, W.; Xu, C.; Ye, D.; Shen, B.; Fan, M. Microstructure characteristics of Wufeng-Longmaxi shale gas reservoirs with different depth, southeastern Sichuan Basin. *Pet. Geol. Exp.* **2020**, *42*, 378–386.

15. Wang, G.; Jiang, Z.; Tong, Y.; Zhao, C.; Luo, Y. Characterization of multi-scale fault system in mountain shale gas reservoirs and its application in Zijinba YS Block of Zhaotong National Shale Gas Demonstration Area. *Nat. Gas Ind.* **2021**, *41*, 14–23.
16. Rui, J.; Wang, C.; Zhang, F.; Yao, Y.; Guo, N.; Zheng, R. Characterization of micro-pore throats in the shale gas reservoirs of Zhaotong National Shale Gas Demonstration Area. *Nat. Gas Ind.* **2021**, *41*, 78–85.
17. Wang, Y.; Dong, D.; Li, X.; Huang, J.; Wang, S.; Wu, W. Stratigraphic sequence and sedimentary characteristics of Lower Silurian Longmaxi Formation in Sichuan Basin and its peripheral areas. *Nat. Gas Ind.* **2015**, *2*, 222–232. [[CrossRef](#)]
18. He, Y.; Huang, X.; Wang, J.; Li, L. Stereoscopic development of shallow shale gas in the Taiyang Block of Zhaotong National Shale Gas Demonstration Area. *Nat. Gas Ind.* **2021**, *41*, 138–144.
19. Zhang, J.; Xu, Y.; Zou, C.; Mei, J.; Xu, Z.; Jiang, L.; Jia, D.; Lu, H. Analysis on the geological conditions for shallow shale gas accumulation: A case study on Linfeng syncline in Zhaotong National Shale Gas Demonstration Area. *Nat. Gas Ind.* **2021**, *41*, 36–44.
20. Xu, Z.; Liang, X.; Lu, H.; Zhang, J.; Shu, H.; Xu, Y.; Wu, J.; Wang, G.; Lu, W.; Tang, X.; et al. Structural deformation characteristics and shale gas preservation conditions in the Zhaotong National Shale Gas Demonstration Area along the southern margin of the Sichuan Basin. *Nat. Gas Ind.* **2019**, *39*, 22–31. [[CrossRef](#)]
21. Zhu, H.; Jia, A.; Wei, Y.; Jia, C.; Jin, Y.; Yuan, H. Characteristics of microscopic pore structure and methane adsorption capacity of shale in the Longmaxi Formation in the Zhaotong area. *Pet. Geol. Recovery Effic.* **2018**, *25*, 1–6.
22. Sun, P.; Zhu, H.; Xu, H.; Hu, X.; Tian, L. Factors affecting the nanopore structure and methane adsorption capacity of organic-rich marine shales in Zhaotong area, Southern Sichuan Basin. *Interpretation* **2020**, *8*, T403–T419. [[CrossRef](#)]
23. Liang, X.; Xu, Z.; Zhang, J.; Zhang, C.; Li, Z.; Jiang, P.; Jiang, L.; Zhu, D.; Liu, C. Key efficient exploration and development technologies of shallow shale gas: A case study of Taiyang anticline area of Zhaotong National Shale Gas Demonstration Zone. *Acta Pet. Sin.* **2020**, *41*, 1033–1048.
24. GB/T21650 2-2008; Pore Size Distribution and Porosity of Solid Materials by Mercury Porosimetry and Gas Adsorption—Part 2: Analysis of Mesopores and Macropores by Gas Adsorption. National Standardization Management Committee: Beijing, China, 2008.
25. Schmitt, M.; Fernandes, C.P.; da Cunha Neto, J.A.B.; Wolf Viviane, F.G.; dos Santos, S.S. Characterization of pore systems in seal rocks using nitrogen gas adsorption combined with mercury injection capillary pressure techniques. *Mar. Pet. Geol.* **2013**, *39*, 138–149. [[CrossRef](#)]
26. LeCompte, B.; Franquet, J.A.; Jacobi, D. Evaluation of Haynesville shale vertical well completions with mineralogy based approach to reservoir geomechanics. In Proceedings of the 2009 SPE Annual Technical Conference and Exhibition, SPE 124227, New Orleans, LA, USA, 4–7 October 2009; Volume 10, pp. 4–7.
27. Wang, Y.; Dong, D.; Yang, H.; He, L.; Wang, S.; Huang, J.; Pu, B.; Wang, S. Quantitative characterization of reservoir space in the Lower Silurian Longmaxi Shale, southern Sichuan, China. *Sci. China Earth Sci.* **2014**, *57*, 313–322. [[CrossRef](#)]
28. Zhang, J.; Li, X.; Wei, Q.; Gao, W.; Liang, W.; Wang, Z.; Wang, F. Quantitative characterization of pore-fracture system of organic-rich marine-continental shale reservoirs: A case study of the Upper Permian Longtan Formation, Southern Sichuan Basin, China. *Fuel* **2017**, *200*, 272–281. [[CrossRef](#)]
29. Wang, Y.; Wang, H.; Zhang, C.; Li, X.; Dong, D. Fracture pore evaluation of the Upper Ordovician Wufeng to lower Silurian Longmaxi formations in southern Sichuan Basin, SW China. *Pet. Explor. Dev.* **2017**, *44*, 563–572. [[CrossRef](#)]
30. GB/T19145-2003; Determination for Total Organic Carbon in Sedimentary Rock. National Standardization Management Committee: Beijing, China, 2008.
31. SY/T5163-2010; Analysis Method for Clay Minerals and Ordinary Non-Clay Minerals in Sedimentary Rocks by the X-ray Diffraction. National Energy Administration: Beijing, China, 2010.
32. Schoenherr, J.; Littke, R.; Urai, J.L.; Kukla, P.A.; Rawahi, Z. Polyphase thermal evolution in the Infra-Cambrian Ara Group (South Oman Salt Basin) as deduced by maturity of solid reservoir bitumen. *Org. Geochem.* **2007**, *38*, 1293–1318. [[CrossRef](#)]
33. Loucks, R.G.; Reed, R.M.; Ruppel, S.C.; Hammes, U. Spectrum of pore types and networks in mudrocks and a descriptive classification for matrix-related mudrock pores. *AAPG Bull.* **2012**, *96*, 1071–1098. [[CrossRef](#)]
34. Thommes, M.; Kaneko, K.; Neimark, A.V.; Olivier, J.P.; Rodriguez-Reinoso, F.; Rouquerol, J.; Sing, K.S. Physisorption of gases, with special reference to the evaluation of the surface area and pore size distribution (IUPAC Technical Report). *Pure Appl. Chem.* **2015**, *87*, 1051–1069. [[CrossRef](#)]
35. Fu, C.; Zhu, Y.; Chen, S. Diagenesis controlling mechanism of pore characteristics in the Qiongzhusi Formation shale, east Yunnan. *J. China Coal Soc.* **2015**, *40*, 439–448.
36. Wang, Y.; Liu, L.; Li, S.; Ji, H.; Xu, Z.; Luo, Z.; Xu, T.; Li, Z. The forming mechanism and process of tight oil sand reservoirs: A case study of Chang 8 oil layers of the Upper Triassic Yanchang Formation in the western Jiyuan area of the Ordos Basin, China. *J. Petrol. Sci. Eng.* **2017**, *158*, 29–46. [[CrossRef](#)]
37. Jarvie, D.M.; Hill, R.J.; Ruble, T.E.; Pollastro, R.M. Unconventional shale-gas systems: The Mississippian Barnett Shale of north-central Texas as one model for thermogenic shale-gas assessment. *AAPG Am. Assoc. Pet. Geol. Bull.* **2007**, *91*, 475–499. [[CrossRef](#)]
38. Hu, H.; Hao, F.; Lin, J.; Lu, Y.; Ma, Y.; Li, Q. Organic matter-hosted pore system in the Wufeng-Longmaxi (O3w-S11) shale, Jiaoshiha area, eastern Sichuan Basin, China. *Int. J. Coal Geol.* **2017**, *173*, 40–50. [[CrossRef](#)]

39. Wang, Y.; Cheng, H.; Hu, Q.; Liu, L.; Hao, L. Diagenesis and pore evolution for various lithofacies of the Wufeng-Longmaxi shale, southern Sichuan Basin, China. *Mar. Pet. Geol.* **2021**, *1133*, 105251. [[CrossRef](#)]
40. Guo, X.; Hu, D.; Li, Y.; Wei, X.; Wang, X.; Zhang, H. Technologies in discovery and exploration of Fuling shale gas field, China. *Nat. Resour.* **2016**, *7*, 271–286. [[CrossRef](#)]
41. Xu, J.; Wu, S.; Liu, J.; Yuan, Y.; Cui, J.; Su, L.; Jiang, X.; Wang, J. New insights into controlling factors of pore evolution in organic-rich shale. *Energy Fuels* **2021**, *35*, 4858–4873. [[CrossRef](#)]